

## **A concurrent two-scale method for modeling jointed structures and their connection failure in the modern vehicle safety analysis**

C. T. Wu<sup>1\*</sup>, Wei Hu<sup>1</sup>, Xiaofei Pan<sup>1</sup>, Masato Nishi<sup>2</sup>, Kei Saito<sup>2</sup>

<sup>1</sup> *Computational and Multi-scale Mechanics Group*

*Livermore Software Technology Corporation, 7374 Las Positas Road, Livermore, CA 94551, USA*

<sup>2</sup> *JSOL Corporation, 1-8-12 Harumi, Chuo-ku, Tokyo 104-6205, Japan*

### **Abstract**

As automotive industry moves rapidly towards electrified and digitalized world, the use of lightweight materials and new joining technologies becomes crucial to counteract the weight of electronic and autonomous equipment for energy efficiency as well as to maintain safety and performance. Numerical modeling the joined structures including their failure behavior has been a big challenge in the modern lightweight vehicle safety design.

In this study, a two-scale method is introduced for modeling jointed structures and their connection failure. In the meso-scale, a new particle stabilization method via a velocity smoothing algorithm is developed for simulating the large deformation and material failure of joint models. The meso-scale joint model characterizing the baseline of joint structure is bridging with macro-scale shell structures using an immerse approach. As a result, a topological coupling between solid and shell formulations is achieved without the need of matching discretization. This two-scale method facilitates the modeling of most connection failures in different joint models and minimizes human interactions with software. A crushing tube example is utilized to demonstrate the effectiveness and applicability of the present method in modeling the joined structures and failure behavior for the modern lightweight vehicle safety design.

*Keywords:* Particle method; Multi-scale; Joint failure; Immersed

---

## **1. Introduction**

Lightweight materials are essential for boosting the fuel economy of conventional cars while maintaining safety and performance. Light-weighting also applies to electric and autonomous vehicles as the use of lightweight materials can offset the weight of batteries, electric motors and autonomous equipment, and at the same time maximize the design for lighter, safer and more efficient vehicles. Lightweight materials like aluminum, advanced high strength steel (AHSS), magnesium, plastic and carbon fiber composites can replace heavy steel in many vehicle parts and have played a critical role in the energy-saving and safety design. The use of multi-material for lightweight structures leads to a dramatic increase in the need to join dissimilar materials for optimizing the overall car design for both mass and performance.

---

\*Corresponding author, C. T. Wu, E-mail: [ctwu@lstc.com](mailto:ctwu@lstc.com)

Over the past decades, computer modeling has been shown to speed up the car design process by simulating experiments. Nowadays, extensive crashworthiness simulation using commercial finite element codes has become a routine during the vehicle's virtual development process before the body-in-white structure is ready for production. In the near future, particular attention also has to be paid to the new structure design of autonomous vehicles to ensure the safety of occupants in the event of emergency braking, crash, electronic failure or even data loss. While thousands of fasteners and joints are used to connect the lightweight structures, those joints are often considered the weakest points as regards to structural strength. When connection failure occurs, the load is shifted from one part to another depending on the types of joints, materials and geometries, which may result in very different deformation results affecting the passenger safety during the vehicle crash. For the electric vehicle, battery crash response plays additional important part of battery and car structure design. Effective design of protective battery pack and its joining technology [Das 2018] has become vital to minimize the risk of thermal runaway during the vehicle crash. Therefore, simulating various connecting failure in lightweight vehicles is an urgent subject [Seeger 2005; Marur 2008; Haufe 2009; Park 2014] for automotive industry.

Among many different joint methods, resistance spot welding (RSW) is the earliest and fully automated joining technique in automotive assembly process for decades. In principle, a full 3D continuum spot weld model [Nielsen 2010] is required in order to capture the complex stress state and the sufficient stiffness responses such as bending and torsional moments in predicting the fracture mode. However, because the finite element model of the body-in-white structure is mainly made of shell elements for efficiency purposes, a coupling of 3D joint elements with shell structures is traditionally simplified through a surface type of connection such as the tied-contact [LS-DYNA]. The respective material failure criterion in those simplified spot weld models are generally derived from coupon tests using optimization methods such as design of experiment (DoE) [Muhammad 2012; Yang 2013]. Hundreds or even thousands of coupon tests including tensile, coach-peel, cross-tension and lap-shear are usually performed to extract the distinct rupture modes from a wide range of deformations for the calibration of material failure model in the tied-contact approach. Unfortunately, this kinematical simplification of joint model using the tied-contact approach and experimental calibration procedure fails to model the pullout rupture [Morawski 2013] which is a governing failure mode when material tearing occurs in the base metal modelled by shell formulations. Although some advanced finite element methods such as extended finite element method (XFEM) [Wu et al. 2018] have been proposed to simulate the crack propagations in shell structures, their applications in connection failure analysis involving complex fracture pattern remain to be accomplished.

On the other hand, automotive industry is striving toward new jointing techniques such as Flow-Drill Screws (FDS), Self-Piercing Riveting (SPR) [Porcaro 2010], etc. for lightweight vehicles as spot welding of lightweight materials is difficult or even impossible. In comparison to spot weld modeling, modeling new types of fasteners and joints is more challenging. In fact, most new joining methods exhibit complicated joint configurations and strong mechanical interlock such that the simple tied-contact approach would be inadequate in producing the desired accuracy to cover complete deformation and failure modes for the car crash analysis. Extant literatures for modeling those new joint models and their failure characteristics are very limited [Hoang 2013; Sonstabo 2016]. It is clear that the tied-contact modeling strategy for treating general connection failures is not sufficient and it could greatly impede the overall accuracy of lightweight car safety design and analysis.

Since the typical tied-contact approach would have a strong restriction to provide an accurate geometrical description and mechanical interlock of the joint model, an appropriate meso-scale model

characterizing the baseline of the joint structure using solid elements is essentially needed. Additionally, because it will be computationally prohibitive to replace shell elements in the whole car body by solid elements in order to model the connection failure, a topological coupling technique between solid and shell elements using non-matching discretization (non-conforming meshes) is also desired. To resolve those intractable numerical issues, the methodology that allows for coupling the meso-scale joint model with macro-scale shell structures is apparently needful. Conventional sub-structure technique [LSDYNA] commonly used in small deformation analysis is obviously not an option for the large deformation problem in connection failure analysis. Other coupling approaches based on the non-intrusive method [Li and Durate 2018; Guinard 2018] requires an iterative process between meso and macro computations, thus not suitable for explicit dynamics analysis in crashworthiness.

Compared to above numerical issues, standard finite element methods pose even more significant problems to simulate the material failure in the meso-scale joint model. Specifically, the  $C^0$ -continuity assumption in most finite element methods is unable to describe the kinematic discontinuity of displacement fields for material separation analysis. Although the element deletion technique can be applied to reduce excessive straining and mesh tangling problems caused by the  $C^0$ -continuity assumption, it gives another instance of numerical instability associated with the loss of conservation properties in terms of mass and linear momentum. As a consequence, the numerical result could become very problematic and parameter sensitive [Wu et al. 2018]. To circumvent this problem, a stable and convergent numerical method capable of simulating large deformation and material failure for different kinds of meso-scale joint models [Wu 2019] will be acquired.

In essence, modeling the connection failure in the car structure is a two-scale problem. Most notably, this two-scale system should be described by a concurrent meso-macro scale model. Figure 1 provides a comprehensive view of Process-Structure-Property-Assembly-Performance loop in the multi-physics and multi-scale vehicle manufacturing and safety simulation in which a two-scale technique for modelling the jointed structures and their failure behavior will be introduced in this study.

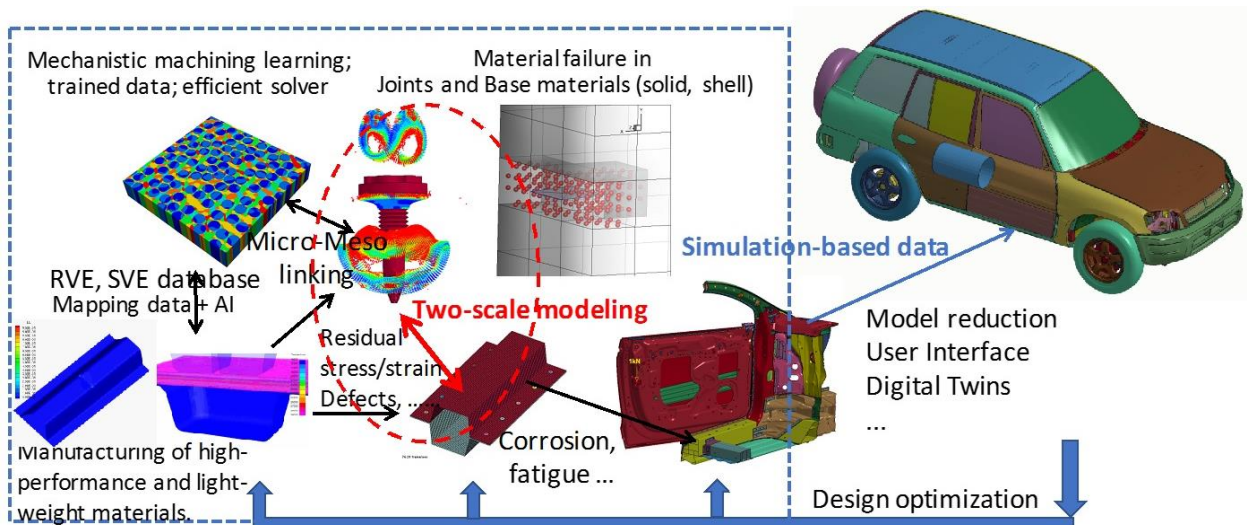


Figure 1. A comprehensive view of Process-Structure-Property-Assembly-Performance loop in the multi-physics and multi-scale vehicle manufacturing and safety simulation

Although the idea of concurrent exchange of information between two scales is not new [Talebi et al. 2014], the development of a two-scale approach for modeling automotive connection failure has not been developed. The objective of this study is to present a two-scale computational method that addresses the critical need in higher-level modeling of different joints and their connection failure behavior for the crash analysis of lightweight vehicles. In the meso-scale, a Lagrangian particle method is employed to simulate the interfacial and pullout ruptures in the 3D continuum joint model. This meso-scale joint model is embedded concurrently into the macro-scale shell structures using a type of kinematical coupling schemes based on the particle immersion technique [Wu et al. 2013, 2016] to achieve the coupling effect, thus bypassing the numerical limitations in the tie-contact approach. The reminder of the paper is organized as follows: In Section 2, the Momentum-consistent Smoothed Particle Galerkin method [Pan 2019; Wu 2019] for simulating the large deformation and material failure in meso-scale joint models is reviewed. Section 3 describes the weak formulation for the two-scale problem using the immerse technique. The implementation procedures are provided in the same section. Numerical examples are given in Section 4, and conclusions are made in Section 5.

## 2. Overview on MC-SPG method for material failure analysis in meso-scale

The Smoothed Particle Galerkin (SPG) method [Wu et al. 2017; 2018] is one of the stabilized Lagrangian particle methods introduced to simulate the extensive plastic deformation and ductile failure for metal fabrication applications [Wu et al. 2018]. The early version of SPG formulation achieves stabilization effects by supplementing the Galerkin form with the stabilizing terms that smooth the oscillation solutions. This necessarily makes SPG method depends upon additional integration points [Wu et al. 2016] whose purpose is to compute the stabilization stress in material nonlinear analysis. Since the stabilization terms were initially derived based on the linear elasticity theory [Wu et al. 2015], a specification of nonlinear stabilization stress [Wu et al. 2018] for the metal plasticity problem is needed in the explicit dynamics analysis. Although the method can sufficiently control spurious energy modes in the nonlinear analysis, it is not computationally efficient.

In order to improve the computational efficiency as well as to avoid the fundamental complication in the stabilization stress calculation, a new version of SPG formulation was recently developed [Pan et al. 2019]. In this new formulation, a velocity smoothing algorithm was introduced to stabilize the solution. It leads to a new stabilization formulation without the use of residual or non-residual stabilization terms [Wu et al. 2017, 2018]. In other words, the new method only requires one integration point per particle and no artificial stabilization control parameter is needed. As a result, the specification of modified tangent modulus and the evaluation of stabilization stresses can be completely bypassed, thus cutting the computational cost. As the new stabilization method is formulated using a smoothed velocity field and is consistently fulfilling the conservation of linear and angular momentum, it was called the Momentum-Consistent Smoothed Particle Galerkin (MC-SPG) method [Wu et al. 2019]. In what follows, the MC-SPG method is used to simulate the pullout rupture of meso-scale joint model in the connection failure analysis. An overview of MC-SPG formulation and its explicit time integration scheme are given as follows (see [Pan et al. 2019; Wu et al. 2019] for detail mathematical derivation and formulations).

### 2.1 Velocity smoothing for stabilization

Let  $\mathbf{X} \in \mathbb{R}^3$  designates the position of a material point in the reference configuration  $\Omega \subset \mathbb{R}^3$ . At time  $t_n$ , let  $\mathbf{x}^n := \boldsymbol{\varphi}^n(\mathbf{X}, t_n)$  be the configuration and  $\mathbf{U}(\mathbf{X})$  be an incremental displacement field, we have

$\boldsymbol{\varphi}^{n+1} = \boldsymbol{\varphi}^n + \mathbf{U}$ . For a particle distribution denoted by an index set  $Z_I = \{\mathbf{X}_I\}_{I=1}^{NP}$ , approximating the velocity field at time  $t_n$  using the first-order meshfree approximation [Wu et al. 2011] gives

$$\dot{\mathbf{u}}^h(\mathbf{X}, t_n) = \sum_{I \in Z_I} \phi_I^a(\mathbf{X}) \hat{\mathbf{u}}_I(\mathbf{X}, t_n) = \sum_{I \in Z_I} \phi_I^a(\mathbf{X}) \hat{\mathbf{u}}_I, \quad \forall \mathbf{X} \in \Omega \quad (1)$$

where  $NP$  is the total number of particles in the discretization.  $\phi_I^a(\mathbf{X}), I = 1, \dots, NP$  can be regarded as the Lagrangian shape functions for velocity field  $\dot{\mathbf{u}}^h$  where the superscript “ $a$ ” denotes the support size of particle  $I$ .  $\hat{\mathbf{u}}_I$  denotes the unsmoothed (oscillating) velocity at particle  $I$ . The oscillating of particle velocity implies spurious energy modes in the displacement field which is resulting from the use of the direct nodal integration (DNI) scheme [Chen et al. 2000] for weak form equations.

To smooth the oscillating velocity field, an introduction of a smoothed velocity field  $\dot{\mathbf{u}}_I$  is defined by [Wu et al. 2019]

$$\begin{aligned} \dot{\mathbf{u}}_I = \dot{\mathbf{u}}(\mathbf{X}_I) &:= \frac{\mathbf{P}_I}{m_I} = \frac{\sum_{J \in Z_I} \hat{m}_J \phi_I^a(\mathbf{X}_J) \hat{\mathbf{u}}_J}{\sum_{J \in Z_I} \hat{m}_J \phi_I^a(\mathbf{X}_J)} = \sum_{J \in Z_I} \left( \frac{\hat{m}_J \phi_I^a(\mathbf{X}_J)}{\sum_{K \in Z_I} \hat{m}_K \phi_I^a(\mathbf{X}_K)} \right) \hat{\mathbf{u}}_J \\ &= \sum_{J \in Z_I} \psi_I^a(\mathbf{X}_J) \hat{\mathbf{u}}_J, \quad \forall \mathbf{X}_I \in Z_I \end{aligned} \quad (2)$$

with

$$\psi_I^a(\mathbf{X}_J) = \frac{\hat{m}_J \phi_I^a(\mathbf{X}_J)}{\sum_{K \in Z_I} \hat{m}_K \phi_I^a(\mathbf{X}_K)} \quad (3)$$

where  $\psi_I^a$  is the velocity smoothing function.  $\mathbf{P}_I$  is the smoothed linear momentum of particle  $I$  defined by

$$\mathbf{P}_I := \sum_{J \in Z_I} \hat{m}_J \phi_I^a(\mathbf{X}_J) \hat{\mathbf{u}}_J \quad (4)$$

$\hat{m}_J$  denotes the unsmoothed lumped mass [Wu et al. 2019] of particle  $J$ . Like most Lagrangian particle methods, the particle mass  $\hat{m}_J$  is fixed through time in MC-SPG method. Analogously, we can also define the smoothed and lumped particle mass using  $\hat{m}_J$  to yield

$$m_I := \sum_{J \in Z_I} \hat{m}_J \phi_I^a(\mathbf{X}_J) \quad (5)$$

We now proceed to update the field variables at particles. Using the central difference integration scheme, the smoothed particle velocity  $\dot{\mathbf{u}}_I$  is computed using Eq. (2) to give

$$\dot{\mathbf{u}}_I^{n+1/2} = \sum_{J \in Z_I} \psi_I^a(\mathbf{X}_J) \hat{\mathbf{u}}_J^{n+1/2} \quad (6)$$

Consequently, the particle displacements are updated using Eq. (6) by

$$\mathbf{u}_I^{n+1} = \mathbf{u}_I^n + \Delta t_{n+1/2} \dot{\mathbf{u}}_I^{n+1/2} \quad (7)$$

where  $\Delta t_{n+1/2} = t_{n+1} - t_n$ . The particle strain rate  $\dot{\boldsymbol{\epsilon}}_I = \nabla^s(\dot{\mathbf{u}}_I)$  can be computed accordingly using the smoothed particle velocity from Eq. (7). Subsequently, the stress can be updated using the standard constitutive routine. Using Eq. (6), the particle density is updated by the continuity equation as

$$\rho_I^{n+1} = \rho_I^n \left( 1 - \Delta t_{n+1/2} \nabla \cdot \dot{\mathbf{u}}_I^{n+1/2} \right) \quad (8)$$

To compute internal force terms, we need the new particle volume. Using the updated particle density in Eq. (8), the new particle volume can be obtained by

$$V_I^{n+1} = \frac{\hat{m}_I}{\rho_I^{n+1}} \quad (9)$$

Finally, it is necessary to update the unsmoothed particle velocity using Eq. (6) for the next time step. Let's first approximate the increment of unsmoothed particle velocity using the smoothed acceleration from previous time step by

$$\Delta \hat{\mathbf{u}}_I^n \approx \Delta t_n \sum_{J \in Z_I} \phi_J^a(\mathbf{X}_I) \ddot{\mathbf{u}}_J^n \quad (10)$$

where  $\Delta t_n = t_{n+1/2} - t_{n-1/2}$ . The update of unsmoothed particle velocity is then accomplished by

$$\begin{aligned} \hat{\mathbf{u}}_I^{n+1/2} &= \hat{\mathbf{u}}_I^{n-1/2} + \Delta \hat{\mathbf{u}}_I^n \\ &= \hat{\mathbf{u}}_I^{n-1/2} + \Delta t_n \sum_{J \in Z_I} \phi_J^a(\mathbf{X}_I) \ddot{\mathbf{u}}_J^n \end{aligned} \quad (11)$$

It is worthwhile to note that in general  $\phi_I^a(\mathbf{X}_J) \neq \phi_J^a(\mathbf{X}_I)$ . In fact,  $\sum_{J \in Z_I} \phi_I^a(\mathbf{X}_J)$  in Eq. (4) and  $\sum_{J \in Z_I} \phi_J^a(\mathbf{X}_I)$  in Eq. (11) represent two different types of kernel summations, the gather type and the scatter type [Wu et al. 2019], respectively. The gather type of kernel summation [Liu and Liu 2003] is mainly used in meshfree collocation methods such as Smoothed Particle Hydrodynamics (SPH). On the other hand, the scatter type of kernel summation is usually adopted in meshfree Galerkin methods such as Element-free Galerkin method [Belytschko et al. 1994] and Reproducing Kernel Particle Method [Liu et al. 1995]. Although the principle idea of velocity smoothing for stabilization using either one of kernel summations is quite simple and intuitive, any arbitrary smoothing of velocity field without a precaution could lead to a loss of conservation properties for linear and angular momentums. It has been shown [Pan et al. 2019; Wu et al. 2019] that by a specific combination of these two kernel summations as described in Eqs. (1) ~ (11) for the velocity smoothing, MC-SPG method can consistently preserve the linear and angular momentums globally for both semi-discrete and full discrete equations.

## 2.2 Large deformation analysis

As mentioned previously, material failure in meso-scale joint models often involves large deformation and material rupture which need to be addressed carefully in the computation. It is known that standard Lagrangian kernel inevitably causes the numerical breakdown when the total form of deformation gradient,  $\mathbf{F} := \frac{\partial \boldsymbol{\varphi}}{\partial \mathbf{X}}$ , in Lagrangian particle ceases to be invertible during the large deformation analysis. This is similar to the mesh distortion problem in the Lagrangian finite element method. To deal with this problem in the large deformation analysis, the MC-SPG method is endorsed with an adaptive anisotropic Lagrangian kernel [Wu et al. 2016] which allows a recursive update of the deformation gradient when the strict use of total form of deformation gradient is no longer applicable. Following the development in [Wu et al. 2016], an incremental form of deformation gradient is utilized in combination with the adaptive anisotropic Lagrangian kernel in this study. The update of deformation gradient can be written as

$$\mathbf{F}^{n+m} = \mathbf{F}^n + \nabla_{\mathbf{X}}(\mathbf{U}(\mathbf{X})) = (\mathbf{I} + \nabla^n \mathbf{u}) \mathbf{F}^n = \hat{\mathbf{F}}^{n+m} \mathbf{F}^n \quad (12)$$

$$\mathbf{U}(\mathbf{X}) := \mathbf{u}(\boldsymbol{\varphi}^n(\mathbf{X}, t_n)) \quad (13)$$

where  $\nabla_{\mathbf{X}}(\cdot)$  denotes the gradient with respect to  $\mathbf{X} \in \Omega$ , and  $\nabla^n(\cdot)$  is the gradient with respect to  $\mathbf{x}(\mathbf{X}, t_n)$ .  $\mathbf{I}$  is the identity matrix.  $\hat{\mathbf{F}}^{n+m}(\hat{\mathbf{x}})$  is the decomposed deformation gradient, from  $t=t_n$  to  $t_{n+m} \in \mathbb{R}_+$ , computed based on the new reference configuration with the updated anisotropic Lagrangian kernel. It is given by [Wu et al. 2016]

$$\hat{\mathbf{F}}_{ij}^{n+m}(\mathbf{X}_J) = \frac{\partial \hat{x}_i}{\partial \hat{x}_j} = \delta_{ij} + \sum_{l \in Z_I} \frac{\partial \phi_l^a(\hat{\mathbf{X}}_J)}{\partial \hat{\mathbf{X}}_j} \hat{\mathbf{u}}_{il}(\mathbf{X}, t_{n+m}) \quad (14)$$

where  $\hat{\mathbf{x}} = \hat{\mathbf{X}} + \hat{\mathbf{u}}(\mathbf{X}, t_{n+m})$  is a position vector based on the new reference configuration, i.e.,  $\hat{\mathbf{X}} = \mathbf{x}(\mathbf{X}, t_n)$ . The anisotropic Lagrangian kernel is updated constantly over a period of time. The anisotropic shape domain of cubic spline kernel function  $\omega_l^a(\hat{\mathbf{X}}_J)$  [Wu et al. 2011], defined for particle neighbor-search, deforms and rotates according to the Lagrangian motion between each two adaptive Lagrangian kernel steps [Wu et al. 2016]. Using the adaptive anisotropic Lagrangian kernel, the deformation gradient differentiates the incremental form from the total form in numeric. Our numerical experiences suggest that the update procedure combining the incremental form of deformation gradient and adaptive anisotropic Lagrangian kernel is very suitable for the large deformation analysis of metal plasticity problems [Wu et al. 2016; 2018]. We address readers to the reference [Wu et al. 2016] for a comprehensive description of the approach.

### 2.3 Material failure analysis

A bond-based failure algorithm, motivated by the peridynamics approach [Silling 2000] for three-dimensional material failure analysis, has been employed to simulate the ductile failure in SPG method [Wu et al. 2017]. The peridynamics approach introduces material failure through the bond breakage. Given a length of the bond  $\|\mathbf{X}_J - \mathbf{X}_I\|$  for a particle pair consisting of particles  $I$  and  $J$  in the initial configuration, the stretch ratio  $e_{IJ}$  of the bond is defined by

$$e_{IJ} := \frac{\|\mathbf{x}_J - \mathbf{x}_I\|}{\|\mathbf{X}_J - \mathbf{X}_I\|} \quad (15)$$

In brittle fracture analysis, a critical stretch ratio  $e_{crit}$  relating to the fracture energy released rate can be defined [Ren et al. 2017] for bond breakage. However, for most ductile failure, fracture energy released rate is generally not available. In engineering practice, a failure criterion measured by the effective plastic strain is often considered.

Since the bond is a representation of a connection between two particles, two neighboring particles can simply be regarded as disconnected during the neighbor searching when their averaged effective plastic strain reaches a respective critical value. This simplification of bond breakage prompts a bond-based failure algorithm in SPG method [Wu et al. 2017] to model the three-dimensional ductile failure. Consequently, the cubic spline kernel function  $\omega_l^a(\hat{\mathbf{X}}_J)$  used in neighbor-search can be modified by introducing a characteristic function  $\chi(|\hat{\mathbf{X}}_J - \hat{\mathbf{X}}_I|)$  for a pair of particles  $I$  and  $J$  to describe the bond breakage such that

$$\hat{\omega}_l^a(\hat{\mathbf{X}}_J) = \chi(|\hat{\mathbf{X}}_J - \hat{\mathbf{X}}_I|) \omega_l^a(\hat{\mathbf{X}}_J) \quad (16)$$

where

$$\chi(|\hat{\mathbf{X}}_J - \hat{\mathbf{X}}_I|) := \begin{cases} 1, & \text{if } \hat{\mathbf{X}}_J \in \text{supp}(\phi_I^a) \text{ and } (\bar{\varepsilon}_{IJ}^P < \bar{\varepsilon}_{crit}^P \text{ and } e_{IJ} < e_{crit}) \\ 0, & \text{otherwise} \end{cases} \quad (17)$$

$\bar{\varepsilon}_{IJ}^P = (\bar{\varepsilon}^P(\hat{\mathbf{X}}_I) + \bar{\varepsilon}^P(\hat{\mathbf{X}}_J))/2$  represents an averaged effective plastic strain in the bond  $\|\mathbf{X}_J - \mathbf{X}_I\|$ , and  $\bar{\varepsilon}^P$  is the effective plastic strain.  $\bar{\varepsilon}_{crit}^P$  is the critical effective plastic strain for bond breakage. Additionally, we set the stretch ratio  $e_{IJ} < e_{crit} = 1.0$  in our numerical analysis which implies that the bond failure does not occur under compression. This implication is valid for most metal failure process.

It is important to note that the effective plastic strain at each particle increases monotonically during the course of deformation. Because of that, the kinematic disconnection in a particle pair is a permanent and irreversible process. This is a substantial characteristic for the bond-based failure mechanism in metal failure analyses since the non-physical material self-healing issues resulting from generic neighbor searching algorithm can be completely exempted from the material failure simulation. This simplicity and unique computational properties of bond-based failure algorithm make SPG method an attractive numerical tool in ductile metal failure analysis.

### 3. Concurrent two-scale problem

Under the framework of variational formulation, an existing finite element code can be easily modified to embed the meso-scale joint model using SPG method for large scale structural analysis with connection failure.

#### 3.1 Weak form

The variational equations for macro-scale structure and meso-scale joints in a transient dynamic problem can be formulated using the integration by part to find the macro-scale displacement field  $\mathbf{u}^G(\mathbf{X}^G, t) \in V^G = \{\mathbf{u}^G \in H^1(\Omega^G): \mathbf{u}^G = \mathbf{u}_g \text{ on } \partial\Omega_g\}$  and the meso-scale displacement field  $\mathbf{u}^L(\mathbf{X}^L, t) \in V^L = \{\mathbf{u}^L \in H^1(\Omega^L): \mathbf{u}^L = \mathbf{u}^G \text{ on } \partial\Omega_c\}$ , such that for arbitrary variation  $\delta\mathbf{u}^G \in V_0^G = \{\mathbf{u}^G \in H^1(\Omega^G): \mathbf{u}^G = 0 \text{ on } \partial\Omega_g\}$  and  $\delta\mathbf{u}^L \in V_0^L = \{\mathbf{u}^L \in H^1(\Omega^L): \mathbf{u}^L = 0 \text{ on } \partial\Omega_c\}$ , the following equations are satisfied:

$$\int_{\Omega^G/\Omega^L} \rho \ddot{\mathbf{u}}^G \cdot \delta\mathbf{u}^G d\Omega + \int_{\Omega^G/\Omega^L} \boldsymbol{\sigma} : \nabla^s(\delta\mathbf{u}^G) d\Omega = \int_{\Omega^G/\Omega^L} \mathbf{b} \cdot \delta\mathbf{u}^G d\Omega + \int_{\partial\Omega_n} \mathbf{h} \cdot \delta\mathbf{u}^G ds + \int_{\partial\Omega_c} \mathbf{f}^c \cdot \delta\mathbf{u}^G ds \quad (18)$$

$$\int_{\Omega^L} \rho \ddot{\mathbf{u}}^L \cdot \delta\mathbf{u}^L d\Omega + \int_{\Omega^L} \boldsymbol{\sigma} : \nabla^s(\delta\mathbf{u}^L) d\Omega = 0 \quad (19)$$

where  $\Omega^G$  and  $\Omega^L$  denote the macro-scale and meso-scale domains, respectively.  $\mathbf{b}$  is the body force vector and  $\boldsymbol{\sigma}$  is the Cauchy stress obtained from the constitutive law. The  $\partial\Omega_g$  notation describes a Dirichlet boundary imposed by a displacement  $\mathbf{u}_g$  and  $\partial\Omega_n$  is the Neumann boundary prescribed by a surface traction  $\mathbf{h}$  with  $\partial\Omega_g \cap \partial\Omega_n = \emptyset$ .  $\partial\Omega_c$  is the coupling interface of two scales as shown in Fig. 2, where the kinematic constraint equations  $\mathbf{u}^L = \mathbf{u}^G, \dot{\mathbf{u}}^L = \dot{\mathbf{u}}^G$  are imposed in the meso-scale computation and  $\mathbf{f}^c$  is the constrained force computed from the meso-scale.



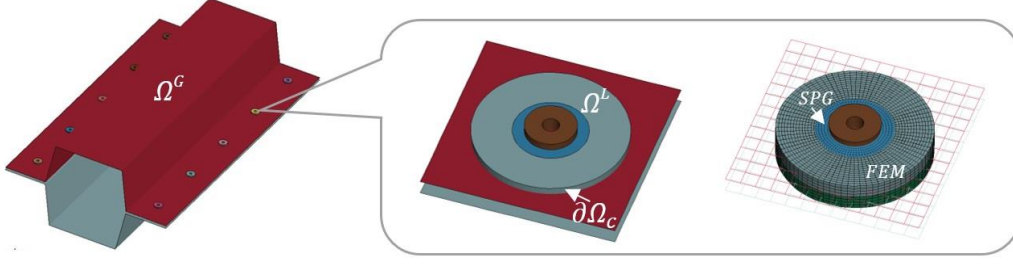


Figure 2. Two-scale models of joints (bolts) in large scale structure

Note that the size of joints is usually much smaller than that of the overall domain in the macro-scale, and the internal energy  $\int_{\Omega^L} \boldsymbol{\sigma} : \nabla^s(\delta \mathbf{u}^G) d\Omega$  is ignorable due to the constraints on the coupling interface  $\partial\Omega_c$ , so that Eq. (18) can be estimated as follows to significantly reduce the meshing and computational cost:

$$\int_{\Omega^G} \rho \ddot{\mathbf{u}}^G \cdot \delta \mathbf{u}^G d\Omega + \int_{\Omega^G} \boldsymbol{\sigma} : \nabla^s(\delta \mathbf{u}^G) d\Omega = \int_{\Omega^G} \mathbf{b} \cdot \delta \mathbf{u}^G d\Omega + \int_{\partial\Omega_n} \mathbf{h} \cdot \delta \mathbf{u}^G ds + \int_{\partial\Omega_c} \mathbf{f}^c \cdot \delta \mathbf{u}^G ds \quad (20)$$

The base material around joints in the meso-scale shown in Fig. 2 has two parts, where the one with severe material deformation and failure is handled by SPG, and the other is modeled by standard FEM solid elements to save CPU time. By substituting the FEM and SPG approximations  $\mathbf{u}^G(\mathbf{X}^G, t) = \sum_I N_I^G(\mathbf{X}^G) \mathbf{U}_I^G(t)$ ,  $\mathbf{u}^L(\mathbf{X}^L, t) = \sum_I \phi_I^L(\mathbf{X}^L) \mathbf{U}_I^L(t)$  into Eqs. (19) and (20), the semi-discrete equations can be expressed by the following algebraic equations

$$\mathbf{M}^G \ddot{\mathbf{U}}^G = \mathbf{F}^{ext} + \mathbf{F}^c - \mathbf{F}_{int}^G \quad (21)$$

$$\mathbf{M}^L \ddot{\mathbf{U}}^L = -\mathbf{F}_{int}^L \quad (22)$$

where

$$\mathbf{M}_{IJ}^G = \int_{\Omega^G} \rho N_I^G N_J^G d\Omega \quad (23)$$

$$\mathbf{F}_I^{ext} = \int_{\Omega^G} \mathbf{b} N_I^G d\Omega + \int_{\partial\Omega_n} \mathbf{h} N_I^G ds \quad (24)$$

$$\mathbf{F}_I^c = \int_{\partial\Omega_c} \mathbf{f}_I^c ds \quad (25)$$

$$\mathbf{F}_{int,I}^G = \int_{\Omega^G} \boldsymbol{\sigma}_0 : \nabla_{\mathbf{X}^G} N_I^G d\Omega \quad (26)$$

$$\mathbf{M}_{IJ}^L = \int_{\Omega^L} \rho \phi_I^L \phi_J^L d\Omega \quad (27)$$

$$\mathbf{F}_{int,I}^L = \int_{\Omega^L} \boldsymbol{\sigma}_0 : \nabla_{\mathbf{X}^L} \phi_I^L d\Omega \quad (28)$$

,  $N^G$  and  $\phi^L$  are approximation functions in the macro and meso scales, respectively.  $\boldsymbol{\sigma}_0$  is the first Piola-Kirchhoff stress tensor.

Considering the non-conforming mesh shown in Fig. 3 at the interface across two scales, the kinematic constraints in the meso-scale are approximated as follows:

$$\mathbf{U}_I^L \equiv \mathbf{U}^L(\mathbf{X}_I^L) = \sum_J N_J^G(\epsilon(\mathbf{X}_I^L)) \mathbf{U}_J^G, \text{ for } \forall \mathbf{X}_I^L \in \partial\Omega_c \quad (29)$$

$$\dot{\mathbf{U}}_I^L \equiv \dot{\mathbf{U}}^L(\mathbf{X}_I^L) = \sum_J N_J^G(\epsilon(\mathbf{X}_I^L)) \dot{\mathbf{U}}_J^G, \text{ for } \forall \mathbf{X}_I^L \in \partial\Omega_c \quad (30)$$

where  $\epsilon(\mathbf{X}_I^L)$  is a projection function mapping  $\mathbf{X}_I^L$  into the macro-scale reference configuration  $\mathbf{X}^G$ . In order to enforce the through-thickness constraints due to the rotational degrees of freedom in the macro-scale shells, Eqs. (29) and (30) need to be modified by

$$\mathbf{U}_I^L \equiv \mathbf{U}^L(\mathbf{X}_I^L) = \sum_J N_J^G(\epsilon(\mathbf{X}_I^L)) \mathbf{U}_J^G + |\epsilon(\mathbf{X}_I^L) - \mathbf{X}_I^L| \Delta \mathbf{n}(\mathbf{X}_I^L, t), \text{ for } \forall \mathbf{X}_I^L \in \partial\Omega_c \quad (31)$$

$$\dot{\mathbf{U}}_I^L \equiv \dot{\mathbf{U}}^L(\mathbf{X}_I^L) = \sum_J N_J^G(\epsilon(\mathbf{X}_I^L)) \dot{\mathbf{U}}_J^G + |\epsilon(\mathbf{X}_I^L) - \mathbf{X}_I^L| \Delta \dot{\mathbf{n}}(\mathbf{X}_I^L, t), \text{ for } \forall \mathbf{X}_I^L \in \partial\Omega_c \quad (32)$$

where  $\mathbf{n}(\mathbf{X}_I^L, t)$  is the unit vector normal to the macro-scale middle plane pointing to the meso-scale material point  $\mathbf{X}_I^L$ . Note that the displacement and velocity for  $\forall \mathbf{X}_I^L \in \partial\Omega_c$  in Eqs. (31) and (32) need to be further updated by  $[\dot{\mathbf{U}}_I^L \cdot \mathbf{n}(\mathbf{X}_I^L, t)] \mathbf{n}(\mathbf{X}_I^L, t)$  to take into account the deformation along the thickness direction.

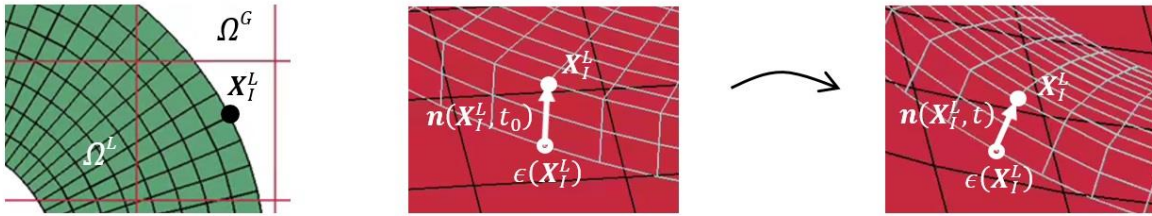


Figure 3. The non-conforming coupling interface between shell (macro-scale) and solid (meso-scale)

The constrained force can be computed by integrating all the contribution from the meso-scale internal force at the coupling interface  $\partial\Omega_c$  as follows:

$$\mathbf{F}_I^c \equiv \mathbf{F}^c(\mathbf{X}_I^G) = \sum_J N_I^G(\epsilon(\mathbf{X}_I^L)) \mathbf{F}_{int,J}^L, \text{ for } \forall \mathbf{X}_I^G \in \partial\Omega_c \quad (33)$$

, and the corresponding constrained moment at the coupling interface  $\partial\Omega_c$  for the macro-scale shell structure is expressed by

$$\mathcal{M}_I^c \equiv \mathcal{M}^c(\mathbf{X}_I^G) = \sum_J N_I^G(\epsilon(\mathbf{X}_I^L)) [|\epsilon(\mathbf{X}_I^L) - \mathbf{X}_I^L| \mathbf{n}(\mathbf{X}_I^L, t) \times \mathbf{F}_{int,J}^L], \text{ for } \forall \mathbf{X}_I^G \in \partial\Omega_c \quad (33)$$

### 3.2 Numerical procedure

Modeling a 3D continuum joint structure in meso-scale requires a refined discretization and consequently smaller time step size ( $\Delta t^G \gg \Delta t^L$ ) in explicit dynamic computation. Instead of imposing the same small time step size on the whole structure, we isolate the computation in meso-scale model but make it run simultaneously with macro-scale structures using the sub-cycling technique. The co-simulation is performed using master/slave setup, where the collective communication between master and slave jobs is

carried out at synchronization points currently through MPI. An adaptor API is called by two scale jobs to exchange data and synchronize the time integration so that the main structure of existing finite element code needs no change to be adopted in both jobs. Figure 4 shows the proposed co-simulation flowchart using central difference time integration scheme.

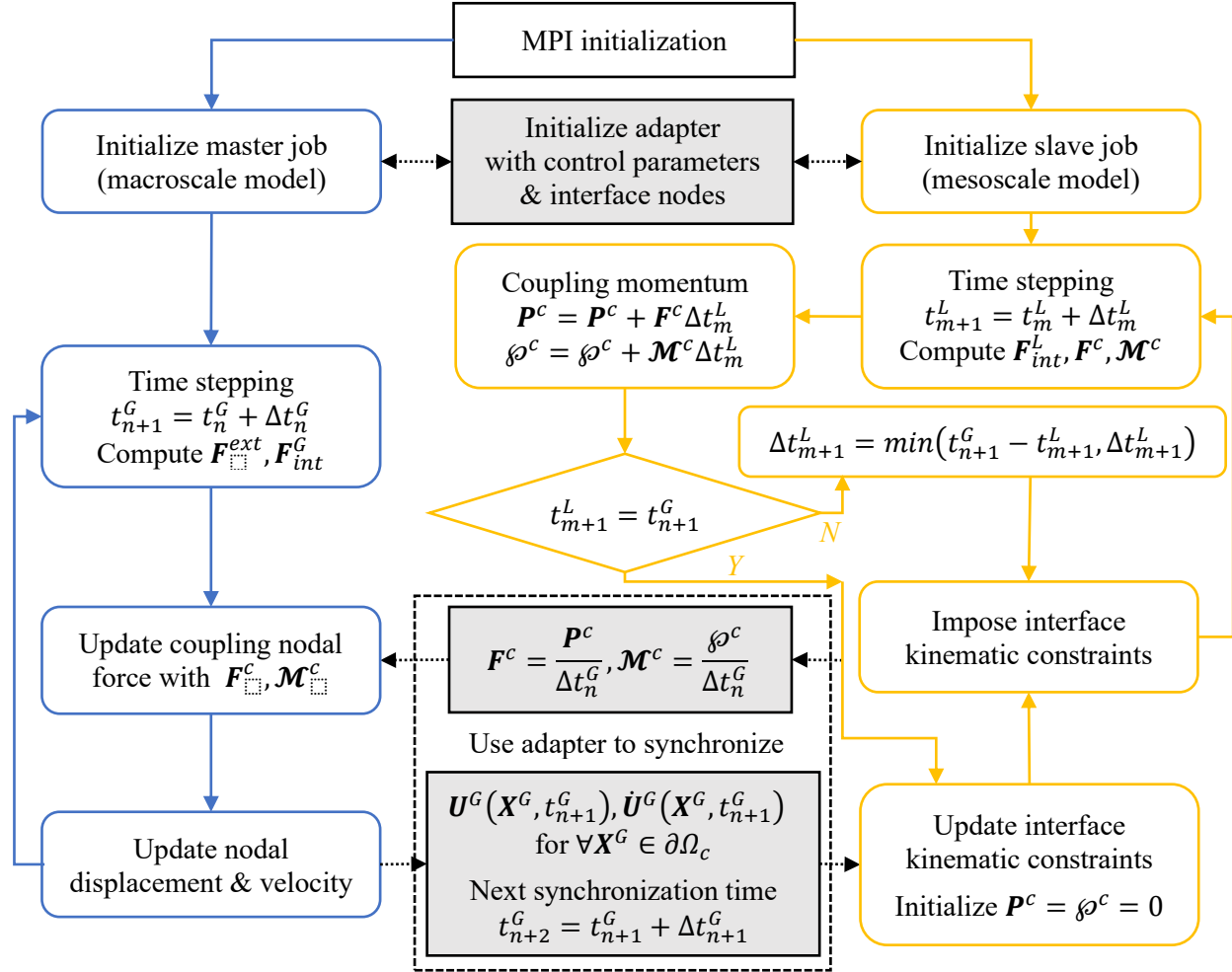


Figure 4. The co-simulation flowchart

## 4. Numerical examples

### 4.1 Simple tension problem

Consider a tension test on a coupon using both single-scale solid and two-scale shell/solid models as shown in Fig 5. The dimension is  $24 \times 8 \times 4 \text{ mm}$  ( $L \times W \times H$ ). The material density is  $7.85 \times 10^{-3} \text{ g/mm}^3$ , the Young's modulus is  $210 \text{ GPa}$  with the yield stress  $1 \text{ GPa}$  and the kinematic hardening  $E_t = 1 \text{ GPa}$ . The constant velocity  $20 \text{ mm/s}$  is applied on both ends. SPG with bond breakage  $\bar{\epsilon}_{crit}^P = 0.5$  is used in the center portion of solid models to better simulate material large deformation and separation. The time step size of the single-scale solid model and macro-scale shell model is  $3.5 \times 10^{-5} \text{ s}$  and that of the meso-scale model is  $8.5 \times 10^{-6} \text{ s}$ . We expect to observe material necking due to plastic deformation in both width and thickness directions using solid formulation.

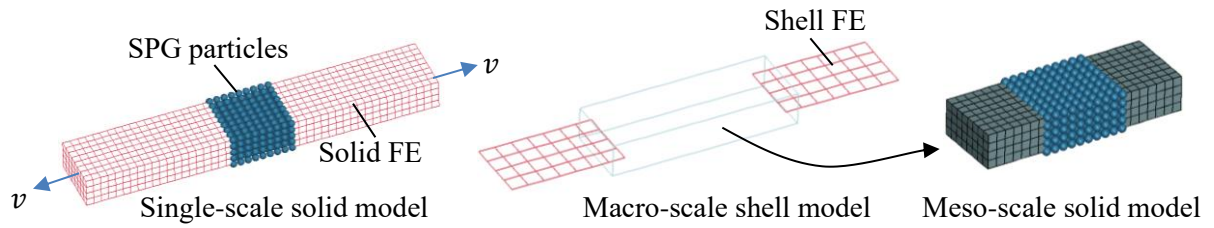


Figure 5. Simple tension test

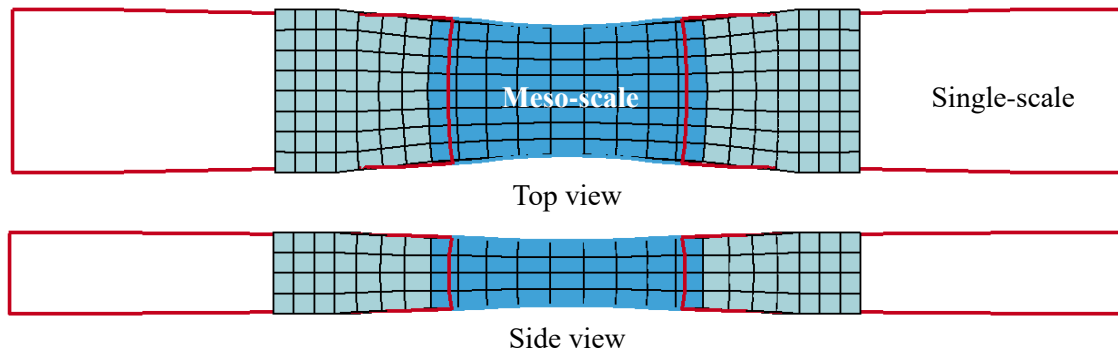


Figure 6. Deformation profile

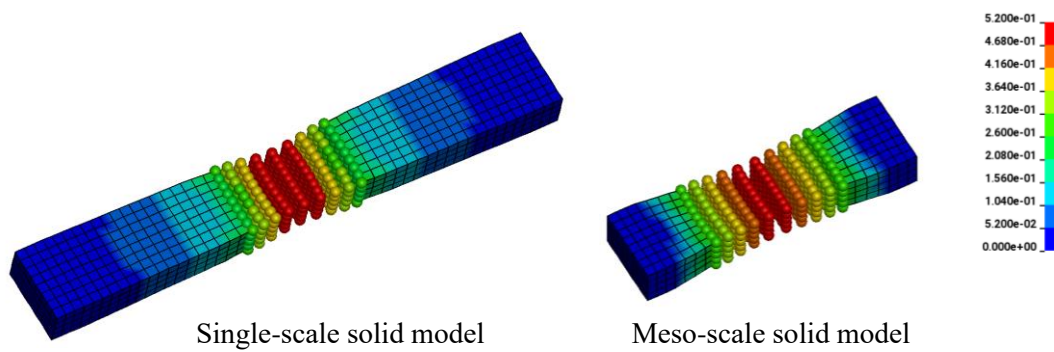


Figure 7. Effective plastic strain (EPS) contour

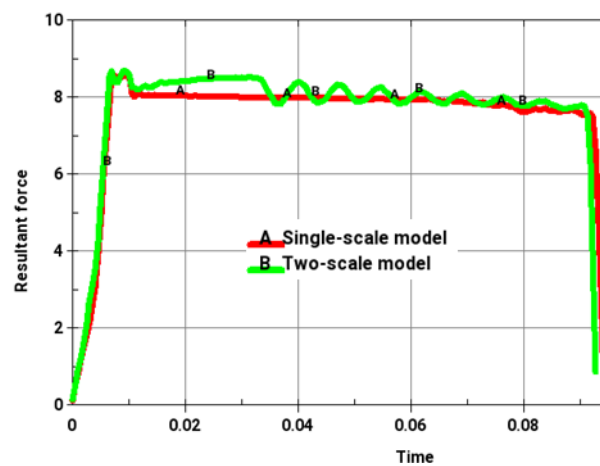


Figure 8. Resultant force curve

Figure 6 shows that the shape of necking obtained by the two-scale model matches the single-scale result very well. The overall distribution of effective plastic strain (EPS) is very similar between two models as shown in Fig. 7 although the meso-scale result is relatively more localized. The meso-scale resultant force curve in Fig. 8 agrees with the single-scale result during the loading process, where the minor oscillation comes from the macro-meso coupling.

#### 4.2 Single connection failure analysis

Consider a single joint (bolt) as shown in Fig. 9, where two shells with  $1mm$  thickness are connected by a rigid bolt. The surrounding base material of the joint is modeled by solids in the meso scale, and SPG with bond breakage  $\bar{\varepsilon}_{crit}^P = 0.1$  is used where the large material deformation and failure is expected to occur. The material density is  $7.85 \times 10^{-3} g/mm^3$ , the Young's modulus is  $210GPa$  with the yield stress  $0.2GPa$  and the kinematic hardening  $E_t = 20GPa$ . The constant velocity  $10mm/s$  is applied on the edges as shown in Fig. 9. The time step size of the macro-scale shell model is  $1.66 \times 10^{-4}s$  and that of the meso-scale model is around  $2.0 \times 10^{-5}s$ .

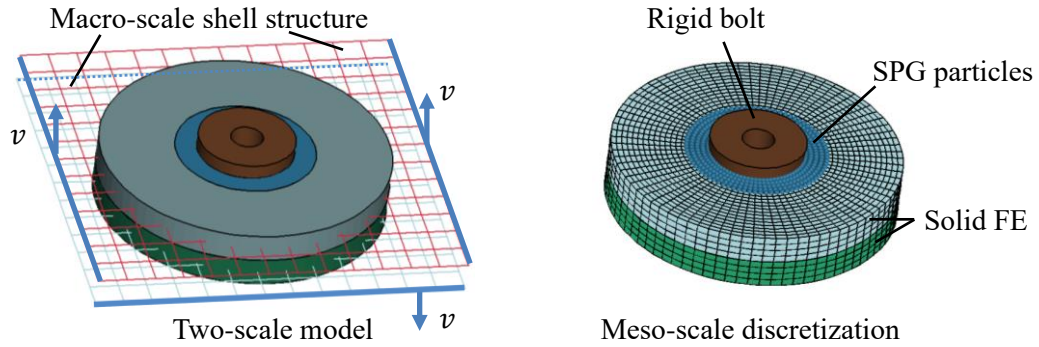


Figure 9. Single joint problem

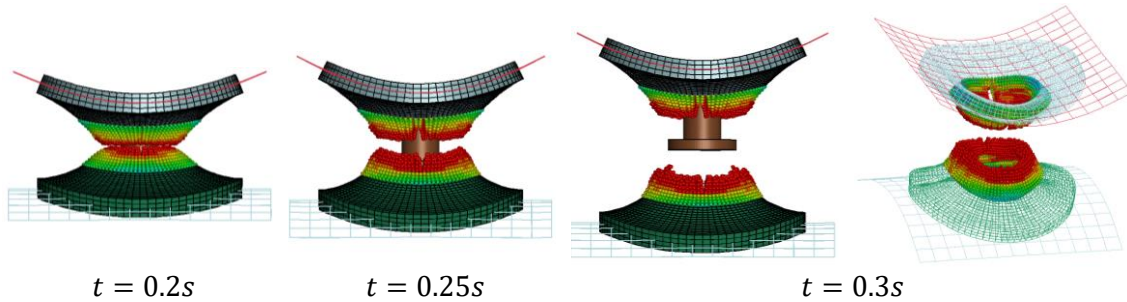


Figure 10. Progressive deformation profile and EPS contour (fringe level 0~0.4)

The progressive plots in Fig. 10 show reasonable deformation in both macro and meso scales and the desirable material failure pattern captured by SPG in the meso scale. Note that the material failure can be simulated only in the meso-scale SPG solids not in the macro-scale shells. The matching of deformation profile at the coupling interface between the meso-scale solids and macro-scale shells in both translational and rotational degrees of freedom indicates that the through-thickness constraints are accurately imposed by the proposed two-scale coupling scheme.



### 4.3 Crash tube analysis

Consider a crash tube problem as shown in Fig. 11, where five pairs of joints fasten two layers of shell structure with  $1\text{mm}$  thickness. The crash tube has one end fixed and the other subjected to a constant velocity  $10\text{mm/s}$ . Ten joints are rigid bolts in the design case I while two joints  $3 - 3'$  are replaced by rigid screws in the case II. The modeling of meso scale joints including the material parameters are the same as the previous example in 4.2. The time step size of the macro-scale shell model varies in  $(1.0 \sim 1.6) \times 10^{-4}\text{s}$ , and that of the meso-scale model falls into the range of  $(1.3 \sim 3.2) \times 10^{-5}\text{s}$  for the case I and  $(1.1 \sim 1.7) \times 10^{-5}\text{s}$  for the case II with smaller mesh size, where the variation of time step sizes is due to the mesh distortion of finite elements as the material deforms.

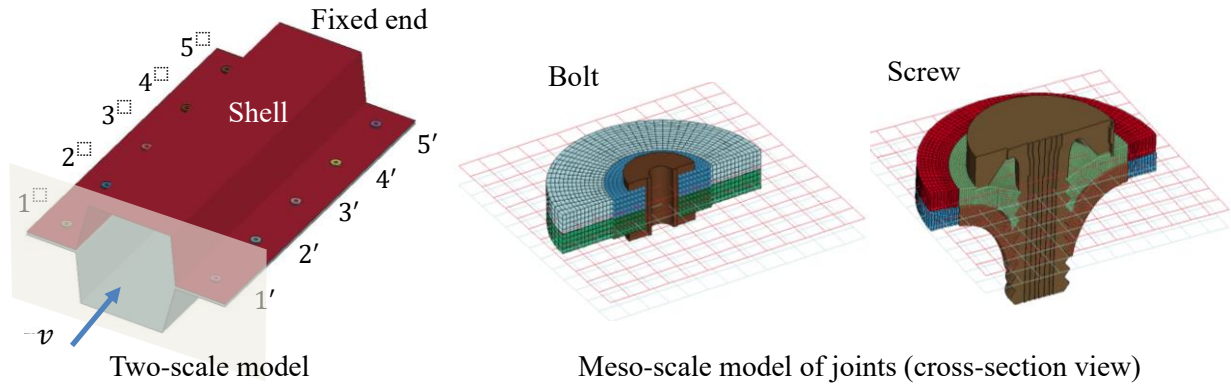


Figure 11. Crash tube problem

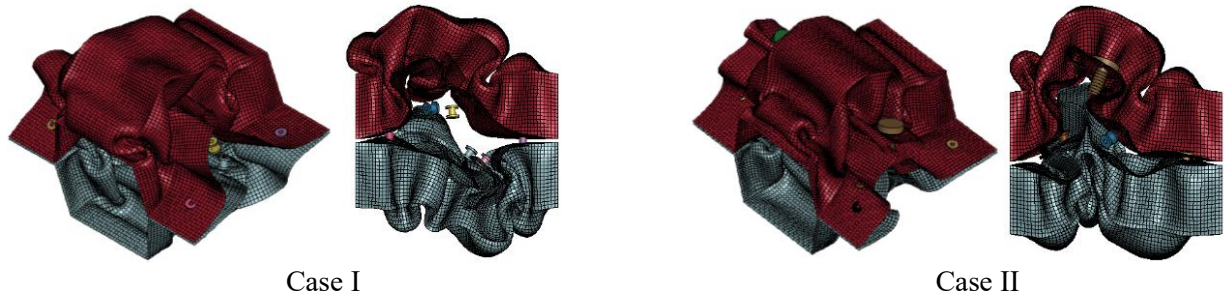


Figure 12. Final deformation profile of crash tube analyses ( $45^\circ$  angle of view and side view)

Figure 12 shows the final deformation of the macro-scale shell structure for both cases, where the case II with stronger screw joints  $3 - 3'$  has better energy-absorption shape. Note that the meso-scale solids including rigid bolts and screws can only interact with the macro-scale shells through the coupling interface, and there is no contact defined between the meso-scale solids and macro-scale shells. Figure 13 shows different failure pattern of joints  $1 \sim 5$  for both cases, and the corresponding jointing force curves are plot in Fig. 14 where we can clearly see the highest peak force at the stronger screw joint 3 in the case II.

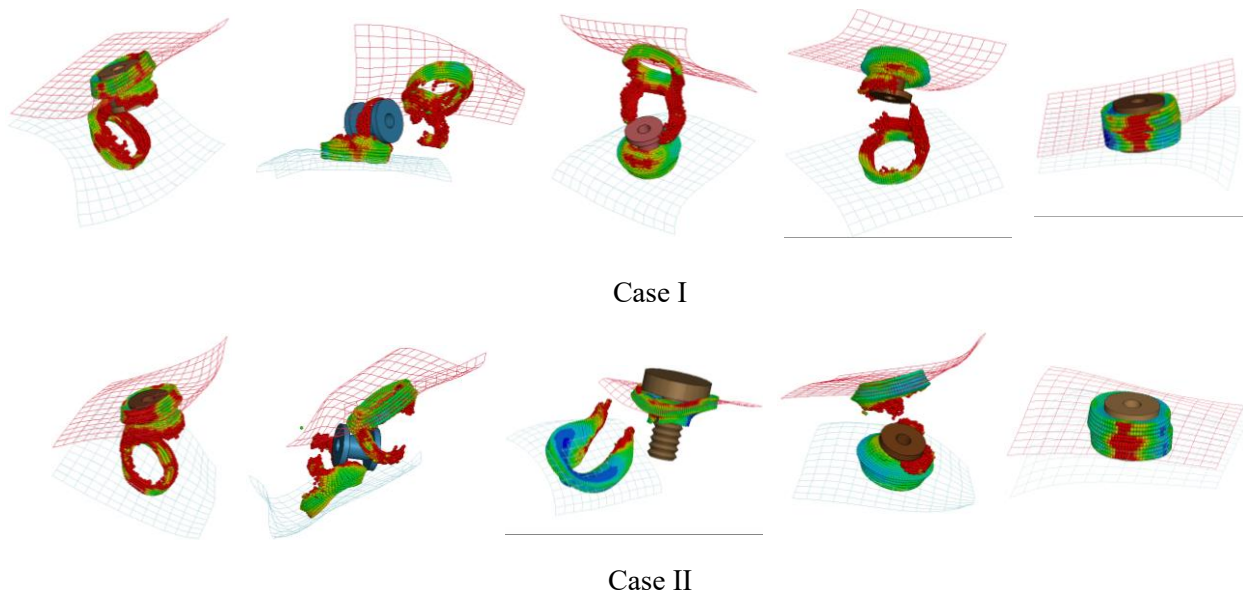


Figure 13. Connection failure with EPS contour (joint ID 1,2,3,4,5 from left to right)

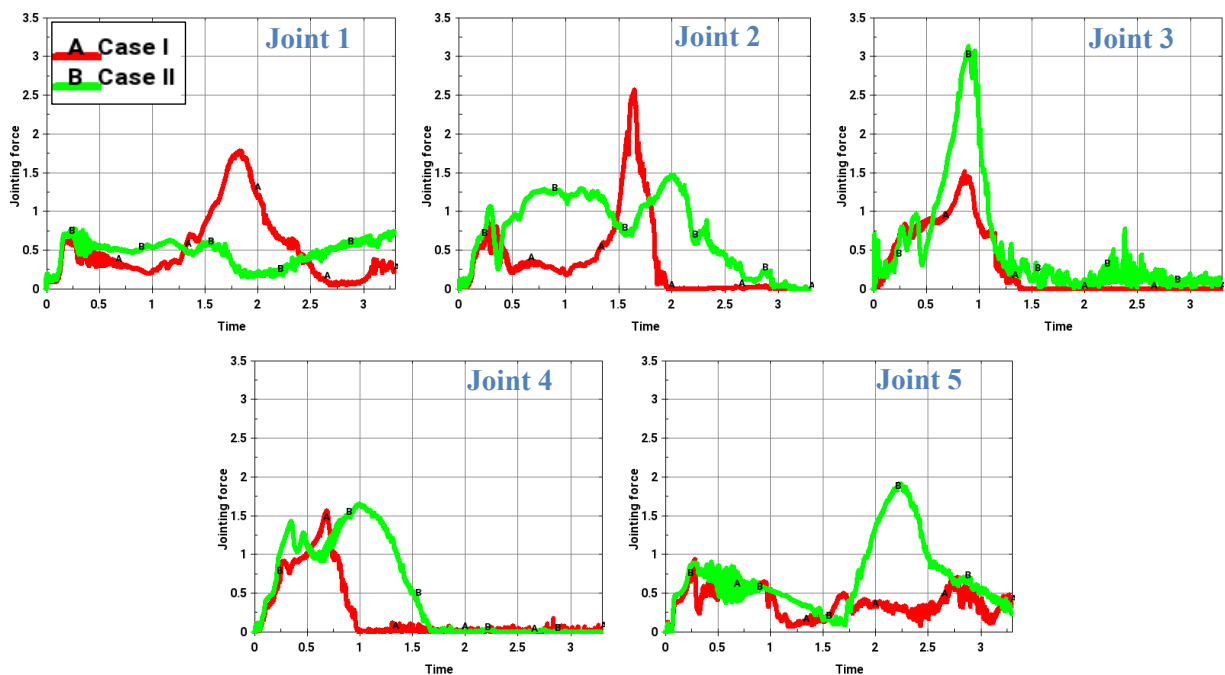


Figure 14. Jointing force curve

## 5. Conclusions

Today's vehicle engineers continue to search for ways to maximize performance and efficiency of new cars. One approach that has gained huge momentum in automotive industry is the light-weighting through advanced material design and fabrication. The integration of stronger, thinner, lighter and mixed materials in new cars has led to significant weight reductions as well as the new jointing technology. On the other hand, inappropriate joining method and unexpected joint failure detected in later stage of new car

development cycle, have frequently resulted in design compromises that can adversely affect weight savings available by using advanced materials. Consequently, further light-weighting opportunities from optimized use of new materials will not be possible without improved joint modeling techniques for the crashworthiness analysis.

Modeling various joints and their failure in a full car finite element model using the tie-contact approach is very time consuming, expansive and error prone. From a vehicle engineer's view point, it is always advantageous to adopt an effective computational model for the simulation of connection failure in crashworthiness analysis. In this study, we have introduced a concurrent two-scale method that is suitable for modeling various joint types and their failure analyses in component design level. Unlike the tie-contact approach where only very few joint models such as spot weld can be idealized to model certain connection failure modes, the present two-scale approach captures meso-structure evolution which is applicable for modeling most connection failures modes in different joint models. Although we have focused on the pullout rupture in this study, the consideration of interfacial rupture in the simulation is not limited by the proposed method. The numerical results in this study suggest that the present method is able to produce the desired pullout rupture mode in the connection failure analysis. Using this two-scale approach, vehicle engineers will be able to set up joint models easily in the finite element car assembly process. This nice feature of present method can minimize human interactions with software and enable more parallel and collaborating engineering work. It is also beneficial to vehicle engineers in analyzing the joining effect of car crash model and to improve the structure integrity during the vehicle virtual development stage. To the authors' best knowledge, other existing technology has not been able to demonstrate similar capability in automotive crash analysis.

Although the present method is studied exemplarily in the component design level, its extension to the full car crashworthiness analysis will not be technically difficult. It requires the establishment of a comprehensive database containing all necessary information for a variety of meso-scale joint models. It also requires the design of scripting functionalities in a dedicated graphical user interface for pre- and post-processing. Those developments will be discussed in the near future.

## Acknowledgements

The authors wish to thank Dr. John O. Hallquist of Livermore Software Technology (LST) LLC for his support to this research. The support from Engineering Technology Division of JSOL Corporation, Japan, is also gratefully acknowledged.

## References

- [1] T. Belytschko, Y.Y. Lu, L. Gu, Element-free Galerkin Methods, *Int. J. Numer. Methods Eng.* 37 (1994) 229-256.
- [2] Y.J. Chao, Failure mode of spot welds: interfacial versus pullout, *Sci. Technol. Weld. Joi.* 8 (2003) 133-137.
- [3] J.S. Chen, C.T. Wu, S. Yoon, Y. You, A stabilized conforming nodal integration for Galerkin Meshfree methods, *Int. J. Numer. Methods Engrg.* 50 (2001) 435-466.
- [4] Abhishek Das, Dezhi Li, David Williams, David Greenwood, Joining Technologies for Automotive Battery Systems Manufacturing, *World Electric Vehicle Journal* 9 (2018) 22; doi:10.3390/wevj9020022
- [5] S. Guinard, R. Bouclier, M. Toniolli, J.C. Passieux, Multiscale analysis of complex aeronautical structures using robust non-intrusive coupling, *Adv. Model. and Simul. in Eng. Sci.*, 5 (2018) 1-27.
- [6] J.O. Hallquist (2006) LS-DYNA Theory Manual. Livermore Software Technology Corporation.
- [7] A. Haufe, M. Feucht, F. Neukamm, The challenge to predict material failure in crashworthiness applications: Simulation of producibility to serviceability. In: Hiermaier S. (eds) *Predictive Modeling of Dynamic Process*,



- Springer, Boston, MA, 2009.
- [8] N.H. Hoang, O.S. Hopperstad, M. Langseth, I. Westermann, Failure of aluminum self-piercing rivets: An experimental and numerical study, *Materials and Design*, 49 (2013) 323-335.
  - [9] H. Li and C.A. Durate, A two-scale generalized finite element method for parallel simulations of spot welds in large structures, *Comput. Methods Appl. Mech. Engrg.*, 337 (2018) 28-65.
  - [10] W.K. Liu, S. Jun, S. Li, J. Adee, T. Belytschko, Reproducing kernel particle methods for structural dynamics, *Int. J. Numer. Methods Eng.* 38 (1995) 1655-1679.
  - [11] G.R. Liu, M.B. Liu, *Smoothed Particle Hydrodynamics*. (2013) World Scientific, Singapore.
  - [12] P.R. Marur, S. Srinivas, A reduced-order finite element model for the simulation of automotive side structure crash response, *Int. J. Crashworthiness* 13 (2008) 211-218.
  - [13] J. Morawski, B. Lauterbach, I. Schwarzer, L. Ramon-Villalonga, M. Tryfonidis, Spot weld modelling with implemented rupture criteria, *Proceedings of the 5<sup>th</sup> ANSA &  $\mu$ ETA International Conference*, Thessaloniki, Greece, 2013.
  - [14] N. Muhammad, Y. HP Manurung, Design parameters selection and optimization of weld zone development in resistance spot welding, *Int. J. Ind. Manuf. Eng.* 6 (2012) 2464-2469.
  - [15] K.L. Nielsen, V. Tvergaard, Ductile shear failure or plug failure of spot welds modelled by modified Gurson model, *Eng. Fract. Mech.* 77 (2010) 1031-1047.
  - [16] E. O’Keefe, J. Imbert-Boyd, M. Worswick, C. Butcher, S. Malcolm, J. Dykeman, P. Penner, C. Yau, R. Soldaat, W. Bernert, Examination of Mode I loading on resistance spot weld groups in tailored hot stampings, *Procedia Eng.* 197 (2017) 294-303.
  - [17] X. Pan, C.T. Wu, W. Hu, Y. Wu, A momentum-consistent stabilization algorithm for Lagrangian particle methods in the thermo-mechanical friction drilling analysis, *Comput. Mech.* (2019) in press.
  - [18] C.K. Park, C.D. Kan, W.T. Hollowell, Evaluation of crashworthiness of a carbon-fiber-reinforced polymer (CFRP) ladder frame in a body-on-frame vehicle, *Int. J. Crashworthiness* 19 (2014) 27-41.
  - [19] R. Porcaro, A.G. Hassen, A. Aalberg, M. Langseth, Jointing of aluminum using self-piercing riveting: Testing, modeling and analysis, *Int. J. Crashworthiness* 13 (2010) 141-154.
  - [20] M. Pouranvari, S.P.H. Marashi, Critical review of automotive steels spot welding: process, structure and properties, *Sci. Technol. Weld. Joi.* 18 (2013) 361-403.
  - [21] B. Ren, C.T. Wu, E. Askari, A 3D discontinuous Galerkin finite element method with the bond-based peridynamics model for dynamics brittle failure analysis, *Int. J. Impact Engrg.* 99 (2017) 14-25.
  - [22] J. Šašel, M. Pašek, K. Beneš, V. Glac, Effects of manufacturing process in crash simulations, *App. Comput. Mech.* 4 (2010) 113-120.
  - [23] F. Seeger, M. Feucht, T.H. Frank, B. Keding, A. Haufe, An investigation on spot welding modeling for crash simulation with LS-DYNA, *Proceedings of the 2005 LS-DYNA Forum*, Bamberg, Germany, 2005.
  - [24] S.A. Silling, Reformulation of elasticity theory for discontinuities and long-range forces, *J. Mech. Phys. Solids* 48 (2000) 175–209.
  - [25] J.K. Sonstabo, D. Morin, M. Langseth, Macroscopic modeling of flow-drill screw connections in thin-walled aluminum structures, *Thin-Walled Structures*, 105 (2016) 185-206.
  - [26] H. Talebi, M. Silani, S.P.A. Bordas, P. Kerfriden, T. Rabczuk, A computational library for multiscale modeling of material failure, *Comput. Mech.* 53 (2014) 1047-1071.
  - [27] C.T. Wu, T.Q. Bui, Y. Wu, T.L. Luo, M. Wang, C.C. Liao, P.Y. Chen, Y.S. Lai, Numerical and experimental validation of a particle Galerkin method for metal grinding simulation. *Comp. Mech.* 61 (2018) 365-383.
  - [28] C.T. Wu, S.W. Chi, M. Koishi, Y. Wu, Strain gradient stabilization with dual stress points for the meshfree nodal integration method in inelastic analysis, *Int. J. Numer. Methods Engrg.* 107 (2016) 3-30.
  - [29] C.T. Wu, Y. Guo, E. Askari, Numerical modeling of composite solids using an immersed meshfree Galerkin method, *Compos. Part B: Eng.* 45 (2013) 1397-1413.
  - [30] C.T. Wu, M. Koishi, W. Hu, A displacement smoothing induced strain gradient stabilization for the meshfree Galerkin nodal integration method, *Comput. Mech.* 56 (2015) 19-37.
  - [31] C.T. Wu, N. Ma, Y. Guo, W. Hu, K. Takada, H. Okada, K. Saito, A dynamic ductile failure analysis of shell

- structures using a nonlocal XFEM method with experimental validation, *Adv. Eng. Softw.* 123 (2018) 1-12.
- [32] C.T. Wu, C.K. Park, J.S. Chen, A generalized approximation for the meshfree analysis of solids, *Int. J. Numer. Methods Engrg.* 85 (2011) 693-722.
  - [33] C.T. Wu, B. Ren, A stabilized non-ordinary state-based peridynamics for the nonlocal ductile material failure analysis in metal machining process, *Comput. Methods Appl. Mech. Engrg.* 291 (2015) 197-215.
  - [34] C.T. Wu, D.D. Wang, Y. Guo, An immersed particle modeling technique for the three-dimensional large strain simulation of particulated-reinforced metal-matrix composites, *Appl. Math. Model.* 40 (2016), 2500-2513.
  - [35] C.T. Wu, Y. Wu, J.E. Crawford, J.M. Magallanes, Three-dimensional concrete impact and penetration simulations using the smoothed particle Galerkin method, *Int. J. Impact Engrg.* 106 (2017) 1-17.
  - [36] C.T. Wu, Y. Wu, D. Lyu, X. Pan, W. Hu, The momentum-consistent smoothed particle Galerkin (MC-SPG) method for simulating the extreme thread forming in the follow drill screw-driving process, *Comp. Part. Mech.* (2019) Accepted for publication.
  - [37] Y.P. Yang, J. Gould, W. Peterson, F. Orth, P. Zelenak, W. Al-Fakir, Development of spot weld failure parameters for full vehicle crash modeling, *Sci. Technol. Weld. Join.* 18 (2013) 222-231.